

# Recording spikes from a large fraction of the ganglion cells in a retinal patch

Ronen Segev, Joe Goodhouse, Jason Puchalla & Michael J Berry II

To understand a neural circuit completely requires simultaneous recording from most of the neurons in that circuit. Here we report recording and spike sorting techniques that enable us to record from all or nearly all of the ganglion cells in a patch of the retina. With a dense multi-electrode array, each ganglion cell produces a unique pattern of activity on many electrodes when it fires an action potential. Signals from all of the electrodes are combined with an iterative spike sorting algorithm to resolve ambiguities arising from overlapping spike waveforms. We verify that we are recording from a large fraction of ganglion cells over the array by labeling the ganglion cells with a retrogradely transported dye and by comparing the number of labeled and recorded cells. Using these methods, we show that about 60 receptive fields of ganglion cells cover each point in visual space in the salamander, consistent with anatomical findings.

Simultaneous recording from most neurons in a neural circuit has not been accomplished anywhere in the vertebrate brain. The retina is promising for such a systematic study, because its modular organization implies that recording from a small patch of ganglion cells should sample its full functional diversity<sup>1</sup>. Although multi-electrode array technology was developed almost 10 years ago<sup>2</sup>, so far we can record only from small fractions of ganglion cells over the array: about 15% of cells in salamander<sup>2,3</sup> and in rabbit<sup>4</sup>. The limitation is not in recording signals from many ganglion cells, but rather in sorting the signals into spike trains from individual neurons. Despite considerable interest in algorithms designed to improve spike sorting, no general solution has emerged<sup>5–7</sup>. What makes this problem difficult is that several spikes overlap each other in time and thereby produce ambiguous signals.

Here we report the development of a new method of multi-electrode recording and spike sorting that uses a dense array and combines signals from up to 30 electrodes to sort spikes; this method can be thought of as a generalization of tetrode recording<sup>8</sup>. We first find the average voltage pattern on the array when a ganglion cell fires a spike and then use an iterative algorithm to match multiple spike patterns to the raw data. Because every ganglion cell occupies a unique position in space, and because extracellular signals decay rapidly with distance, each ganglion cell produces a unique pattern of activity on the dense array. This unique pattern can be used to identify the source of overlapping spikes, which might appear ambiguous if we were to use only a single electrode.

By retrograde labeling of the ganglion cells, we can compare the number of cells over the array to the number of isolated, single-unit spike trains. This comparison shows that all or nearly all of the retinal ganglion cells in a patch of the retina are recorded. This technical advance promises to yield insights into how populations of ganglion cells encode visual stimuli and how the retinal circuitry processes its visual inputs.

## RESULTS

### Determination of array spacing

Electrical activity was recorded by placing the ganglion cell layer against a planar multi-electrode array of either hexagonal (Fig. 1a) or rectangular geometry (Fig. 1b) in which the electrodes were spaced 30  $\mu\text{m}$  apart. We studied the retina of the salamander, a species that is especially well suited for recording from all of the ganglion cells. In cross-section, the ganglion cells could be seen to form a monolayer with only a thin membrane covering them (Fig. 1c).

The cell density, as determined both by retrograde labeling and by electron microscopy of the optic nerve (Methods), was moderate ( $\sim 1,400$  cells/ $\text{mm}^2$ ) and roughly uniform across the retina. At this density, the average spacing between ganglion cells was about 27  $\mu\text{m}$ , which meant that the array should have an electrode near to every ganglion cell. We measured the amplitude of the voltage deflection when ganglion cells fired an action potential and found that this amplitude could be fit by an exponential function of the distance from the primary electrode (Fig. 1d and Methods). The space constant was  $28 \pm 1$   $\mu\text{m}$ , similar to the 30- $\mu\text{m}$  spacing between electrodes.

### Identification of templates

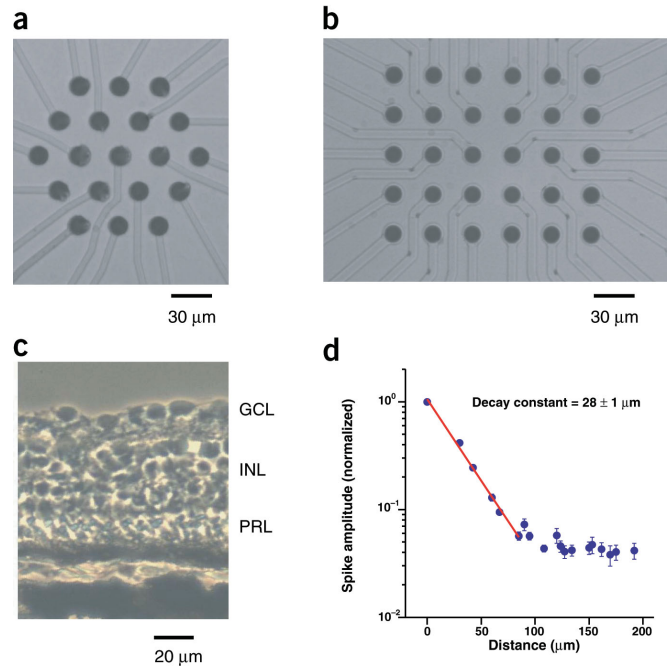
The first step in spike sorting is to find the typical voltage waveform observed on the array when each ganglion cell fires a spike, a pattern that is called the 'spike template'. We found the times when each ganglion cell fired its spike in isolation from the spikes and slow potentials fired from other neurons. The template was an average over all these 'clean' spike waveforms. Although it was easy to identify isolated spikes, they usually comprised a small subset of all of the spikes produced by a ganglion cell, and thus their identification was not by itself sufficient for spike sorting.

Specifically, we started by finding all the times in the raw data that contained a possible spike, which we defined as a voltage

Department of Molecular Biology, Princeton University, Princeton, New Jersey 08544, USA. Correspondence should be addressed to M.J.B. (berry@princeton.edu).

Published online 27 September 2004; doi: 10.1038/nn1323

**Figure 1** The dense array. (a) A planar multi-electrode array with 19 electrodes in a hexagonal geometry. (b) A rectangular array with 30 electrodes. The spacing between adjacent electrodes is 30  $\mu\text{m}$  and the electrode diameter is 10  $\mu\text{m}$ . (c) Cross-section of the tiger salamander retina, showing the main cell layers. GCL, ganglion cell layer; INL, inner nuclear layer; PR, photoreceptor layer. (d) Normalized signal amplitude of spike templates plotted as function of distance to secondary electrodes on which the same spike template was observed. Data (blue dots) are averaged over many spike templates. The exponential curve fit (red line) has a slope of  $28 \pm 1 \mu\text{m}$ , which defines a decay constant.



deflection exceeding 60  $\mu\text{V}$ . This threshold was roughly four times the standard deviation (s.d.) of the voltage on an electrode. We only considered threshold crossings at least 0.4-ms apart to minimize multiple detection of the same spike. For each threshold crossing, we visualized the peak voltage on multiple electrodes by using a version of the open code program Mclust (created by A. Redishi, <http://www.cbc.umn.edu/~redishi/mclust>) that was modified to handle an arbitrary number of electrodes. Clusters were selected manually by using standard constraints, similar to the union and intersection of regions on a plot of peak voltage on one channel versus peak voltage on another channel. The software allowed constraints to be applied across several channels (Fig. 2a,b) and selected a set of voltage waveforms of either 3.2-ms or 6.4-ms duration on all electrodes of the array (Fig. 2c).

This set of waveforms included overlapping spikes from other cells. We selected clean spike waveforms (Fig. 2d) by automated removal of waveforms that differed from the average by more than 2 s.d. and by manual removal of remaining outliers. The average waveform did not change much during the isolation of clean spikes, indicating that the average was relatively insensitive to outliers (a typical example is shown in Fig. 2). Occasionally, the spike waveform changed enough during a burst of spikes that two different clusters of peak voltages were formed. These situations were easy to identify, and the spike trains resulting from the two templates were subsequently combined (see below). Some templates had an amplitude just above the threshold and signal only on the array boundary. These ‘spikelets’ presumably originated from neurons off the array and could not be cleanly isolated.

Spikes were detected by fitting threshold crossing events in the raw data with a linear combination of templates. Each template was allowed to have a shift between  $\pm 1.4 \text{ ms}$  in 0.1-ms steps; we also included a blank template as an option so that small threshold crossing events would not need to be identified as a real spike. All of these template shifts (16 templates with 465 total shifts; Fig. 3) were matched against the raw data by using mean squared error as a measure of goodness of fit. Typically, the three or four smallest values of mean squared error resulted from the same template with successive time shifts, indicating that matches had a temporal precision of about 0.1 ms (Fig. 3a).

Because each threshold crossing event might contain more than one spike, we subtracted the best-fitting shifted template from the raw data and repeated the procedure on the residual (Fig. 3c). In the example shown, the best match on the fourth iteration was the blank template, and the raw voltage waveform was very closely fit by three templates (Fig. 3d). We tested the adequacy of our iterative approach to template matching by exhaustively calculating all possible combinations of up to four templates. In every case, the best match involved the same templates that were chosen by the iterative method. For Figure 3c, the 15 best fits from the exhaustive search involved the same three templates with slightly different temporal shifts.

To guard against using too many templates, we stopped the iterative matching process at a number of templates,  $N$ , that minimized the following heuristic error function (Fig. 3b):

$$E(N) = \left| S - \sum_{i=1}^N T_i \right| + \lambda N$$

Matching templates to the raw data

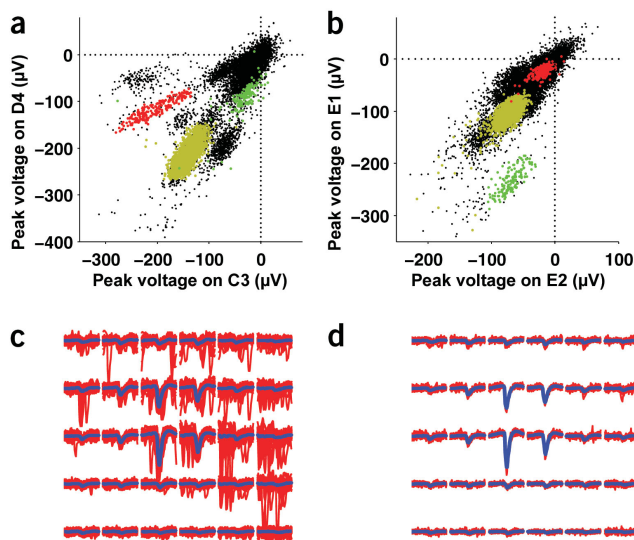
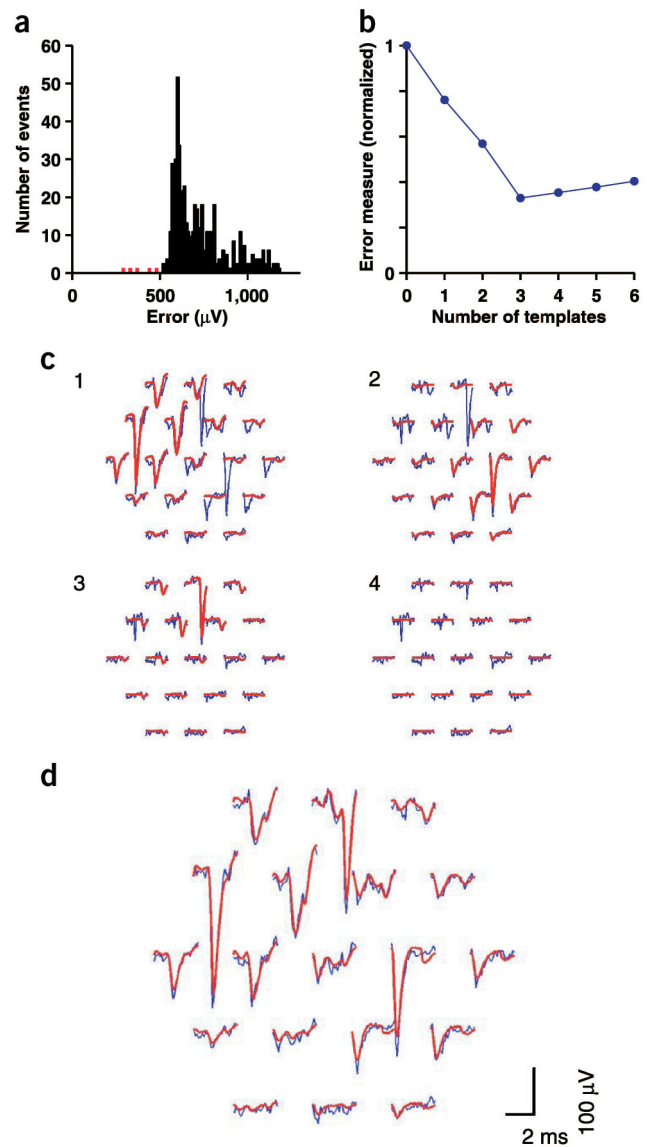


**Figure 2** Identifying spike templates. (a,b) Plots of peak signal amplitude on pairs of electrodes. Three clusters have been defined (red, green and yellow dots). Other clusters have been omitted for clarity. (c) Raw data waveforms from the red cluster in a,b, shown with the average waveform (blue). (d) Subset of clean waveforms (red), shown with the average waveform (blue).



**Figure 3** Matching templates to the raw data. (a) Distribution of error values between a single spike template and a 3.2-ms segment of raw data, compiled over all shifted templates (black bars). The five smallest values come from the same template with successive time shifts (red bars). (b) Normalized error as a function of the number of templates iteratively fit to the raw data. (c) Example of iterative matching for the hexagonal array. After each match, numbered 1–4, the template (red) is subtracted away and a new template is fit to the residual (blue). (d) Resulting fit to the raw data (blue) made with three templates (red). Panels a–d are derived from the same segment of raw data.



where  $S$  is the observed waveform,  $T_i$  is the  $i$ th template, and  $|\dots|$  represents the vector norm of voltages on all channels. The first term is simply the mean squared error between the data and the fit. The second term involves a free parameter  $\lambda$  that adds an incremental cost for using additional templates to explain the observed waveform. This free parameter can be viewed as taking into account the fact that the observation of many overlapping spikes is increasingly improbable<sup>7</sup>.

**Choosing the value of  $\lambda$**

The value of  $\lambda$  was chosen by the requirement that the spike sorting algorithm produced the fewest spike sorting errors. To define errors, we carried out simulations in which we added noise to a spike template and ran our template matching algorithm on the resulting voltage waveforms. We first added gaussian noise with an amplitude (30  $\mu$ V) equal to twice the experimental noise. In this simulation, there were no spike sorting errors at all, indicating that spike templates were distinct and had a high signal-to-noise ratio. This simulation was highly unrealistic, however, because the noise in extracellular recordings is dominated by signals from nearby neurons, known as ‘neural hash’, that are correlated and non-gaussian<sup>9</sup>.

The most realistic noise source are the raw data themselves. A problem with adding templates to the real data is that the spike of that same cell may be present already, which would make an identification of sorting errors ambiguous. To solve this problem, we created virtual templates by taking a real template and shifting all of its signals over by one electrode. To verify that the virtual templates had the same structure as the real templates, we compared the mean squared distances between real templates to those between real and virtual templates and found that the distributions were very similar (data not shown).

In our simulations, we shifted each virtual template by a random time in the range  $\pm 2.8$  ms, clipped the total duration at 6.4 ms, and added a segment of the raw data chosen to include overlapping spikes in their measured frequency. We then ran our matching algorithm and tested whether the virtual template was identified (correct), missing (false negative), or matched with a different template (false positive). As expected, higher values of  $\lambda$  achieved lower numbers of false positives at the expense of introducing more false negatives (Fig. 4f). The minimum total error was found for a  $\lambda$  value of 60–90  $\mu$ V. Here, the percentage of false positives was about 0.4% and that of false negatives was about 0.8%. These error rates are low in comparison to those achieved with tetrode recording<sup>8</sup>.

**Evaluating the method**

To determine the fraction of cells over the array that could be recorded by our methods, we retrogradely labeled the ganglion cells with rhodamine dextran before making the electrical recordings (Methods). Both ganglion cell somas and bundles of axons were visible (Fig. 4a). The number of labeled cells varied considerably from

patch to patch, but we found that a similar number of cells were always recorded (Fig. 4b). On average, about 20% more cells were recorded than labeled, presumably because we sometimes isolated ganglion cells from outside the boundary of the array.

To test for errors in spike sorting, we calculated the fraction of spikes that fell within a 2-ms refractory period. About a third of the cells had absolutely zero refractory violations, and 90% had less than 0.1% violations (Fig. 4e). Using simulations of spike matching, we estimated that the level of false positives in our matching algorithm was about 0.4% (Fig. 4f). These data suggest that we can cleanly isolate spike trains from all or nearly all of the ganglion cells over the array; however, a few factors may lead us to overestimate the fraction of recorded cells.

For example, it is possible that the fluorescent dye was not transported into some of the ganglion cells. To determine the completeness of our retrograde labeling, we also estimated the ganglion cell density by counting axons in the optic nerve (Fig. 4d). The total ganglion cell density estimated in this fashion,  $1,410 \pm 180$  cells/mm<sup>2</sup>, agreed closely with the density of labeled ganglion cell somas,  $1,340 \pm 180$  cell/mm<sup>2</sup> (Fig. 4c).

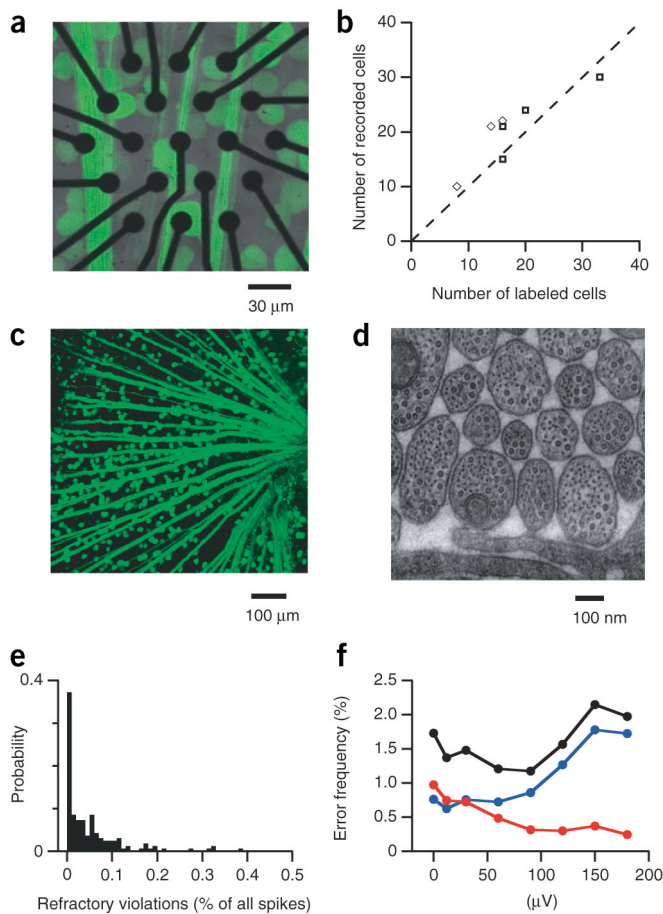


**Figure 4** Evaluating the method. (a) A patch of the salamander retina placed over a hexagonal multi-electrode array. Ganglion cells and axon bundles are fluorescently stained with rhodamine dextran (green); electrodes and leads of the array are black. (b) Number of recorded ganglion cells plotted against the number of fluorescently labeled cells for seven retinal patches; three patches were recorded with the hexagonal array ( $\diamond$ ), four with the rectangular array ( $\square$ ). (c) Larger region of the retina stained with rhodamine dextran. (d) Electron micrograph of a cross-section of the optic nerve. (e) Distribution of the fraction of refractory violations for 164 ganglion cells. (f) Frequency of spike sorting errors plotted against the value of the free parameter  $\lambda$  used in the spike sorting algorithm. Blue, false positives; red, false negatives; black, total error rate.

this layer in the salamander<sup>11–13</sup>, that our array might also sense. Measurement of the intracellular voltage of amacrine cells indicated, however, that many did not fire spikes. For the subset of amacrine cells that do spike, the spike amplitude is rarely greater than 25 mV and the frequency content is in the 0–80 Hz band<sup>14</sup>. We preprocessed the recorded voltages with a band pass filter between 200 and 5,000 Hz, which effectively removed such spike waveforms from our data. In addition, extracellular measurement conditions attenuate intracellular potentials by a factor of about 1,000 (ref. 11), reducing most spikes from amacrine cells well below the noise level of 10–20  $\mu\text{V}$ . Although we cannot rule out the possibility that at some point we have recorded from a spiking amacrine cell, the evidence indicates that this is a very unlikely event and therefore sufficiently rare that it does not appreciably change the estimated fraction of recorded ganglion cells.

A final possibility is that we mistakenly identified two or more templates that actually are the same cell; if so, then our count of recorded cells would be inflated. In such cases, the cross-correlation function between spike trains would have a refractory window, which would persist even after combining the spike trains (Fig. 6). In addition, the receptive field maps of two such spike trains would be nearly identical. For all of these reasons, it was easy to identify double-counted cells and to combine their spike trains together. Spike trains that clearly arose from different cells had distinguishable templates with maximum signal amplitude on different electrodes (Fig. 7a,b) and had clean refractory periods

Another possibility is that some of our isolated spike trains came from axons passing over the array rather than from cell somas. This was not the case, however, because axonal spike waveforms had a characteristic triphasic shape that began with a positive voltage peak (Fig. 5a), whereas somas generated a biphasic spike waveform that began with a negative voltage peak<sup>10</sup> (Fig. 5b). We did record axonal spikes in some retinal patches, but usually could not isolate them cleanly (presumably because of the arrangement of axons into tight bundles; Fig. 4a). In the rare cases in which we could isolate an axonal spike train, these spike trains were observed to have a receptive field far from the array (Fig. 5c).

The ganglion cell layer is known to contain many displaced amacrine cells, accounting for at least 20% of the cells in

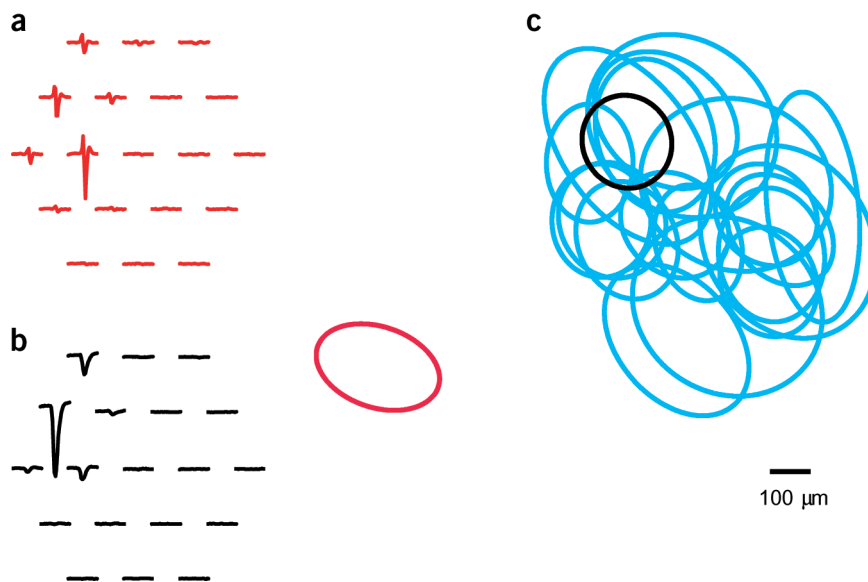


**Figure 5** Axonal versus somatic spikes. (a) Spike template of a cleanly isolated axonal waveform, showing a characteristic triphasic shape. (b) Spike template of a somatic waveform from the same recording. (c) Spatial receptive field profile for the axonal waveform (red), which arises from a location different to that of the spatial profile of the somatic waveform (black), as well as to those of the rest of the somatic spikes in this experiment (cyan).

**Figure 6** Effects of splitting one cell into two templates. A new template, A, was formed by scaling an existing template, B, by a factor of 1.1, and raw data were rematched including the extra template. (a,b) Interspike interval distribution for the spike train from templates A and B, respectively. (c) Interspike interval distribution after combining templates A and B into a single spike train, showing a clear refractory period. (d) Cross-correlation function between spike trains from templates A and B, showing exclusion of time intervals within the refractory period of the neuron. Note that it is more common for the smaller spike (template B) to follow the larger spike, because spike amplitude decreases during a burst.

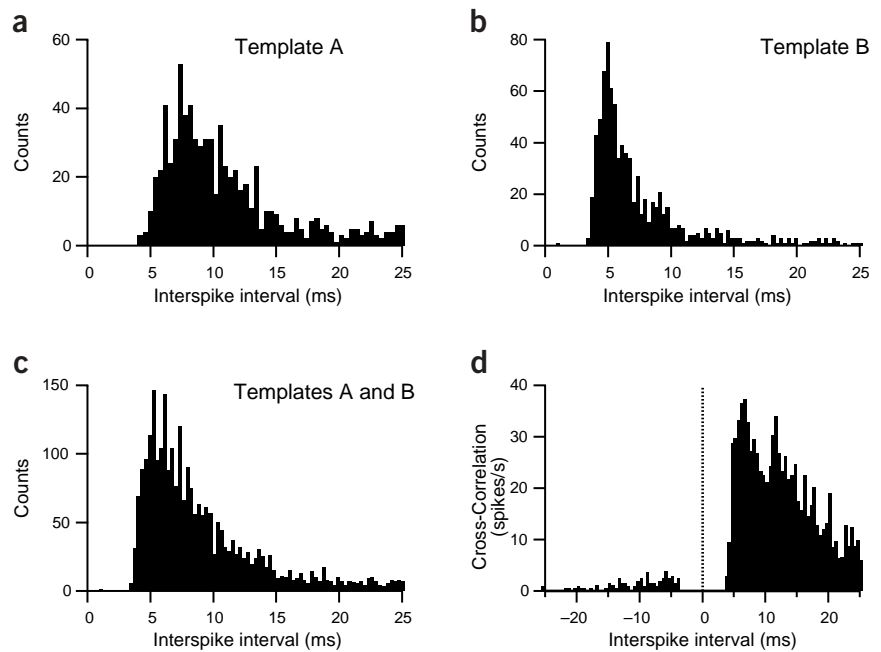


(Fig. 7c,d). When combined together, there were many refractory violations (Fig. 7e) and the cross-correlation function had no refractory window (Fig. 7f).

Taken together, our anatomical and physiological data are consistent with recording all of the ganglion cells over the array. We cannot rule out the possibility that a small fraction of ganglion cells were missed, however, owing to the error bars in our anatomical measurements. We therefore conclude, conservatively, that we have recorded from 80 to 100% of the ganglion cells over the dense array.

**Total coverage of visual space by the ganglion cells**

Because such a large fraction of the ganglion cells over the array are

recorded by our approach, we can obtain a relatively unbiased sampling of the neural population. This is significant, because other electrophysiological techniques that record only a small fraction of nearby neurons are known to have a significant bias in favor of large neurons that produce large extracellular signals<sup>15,16</sup>. We mapped the receptive fields of ganglion cells by using reverse correlation to a flickering checkerboard (Methods). A two-dimensional gaussian provided a good fit to the spatial profile (Fig. 8a,b). We defined the receptive field size of a ganglion cell using the 1σ contour from the gaussian curve fit (Methods). The distribution of receptive field sizes of 103 ganglion cells recorded from three retinas had three overlapping peaks (Fig. 8c), consistent with three broad classes of dendritic field size that have been observed anatomically<sup>17</sup>.

We computed the total coverage factor of the ganglion cell population by multiplying the average receptive field area with the measured cell density (1,410 cells/mm<sup>2</sup>). This quantity measures the number of ganglion cell receptive fields that look at every point in visual space. The total coverage factor was 59 ± 5 (mean ± s.e.m., n = 3 retinas), indicating that the retina uses a highly parallel population code to represent even the sharpest features of a visual image. This total coverage factor is consistent with the total coverage of ganglion cell dendritic fields observed anatomically in several species<sup>17–20</sup>.

**DISCUSSION**

We have introduced a new recording technique based on a dense multielectrode array—which can record signals from a ganglion cell’s spike on many electrodes—along with a multichannel spike-sorting algorithm. By using this technique, we can resolve ambiguities arising from overlapping spike waveforms and thus isolate spike trains from all or nearly all of the ganglion cells over the dense array.

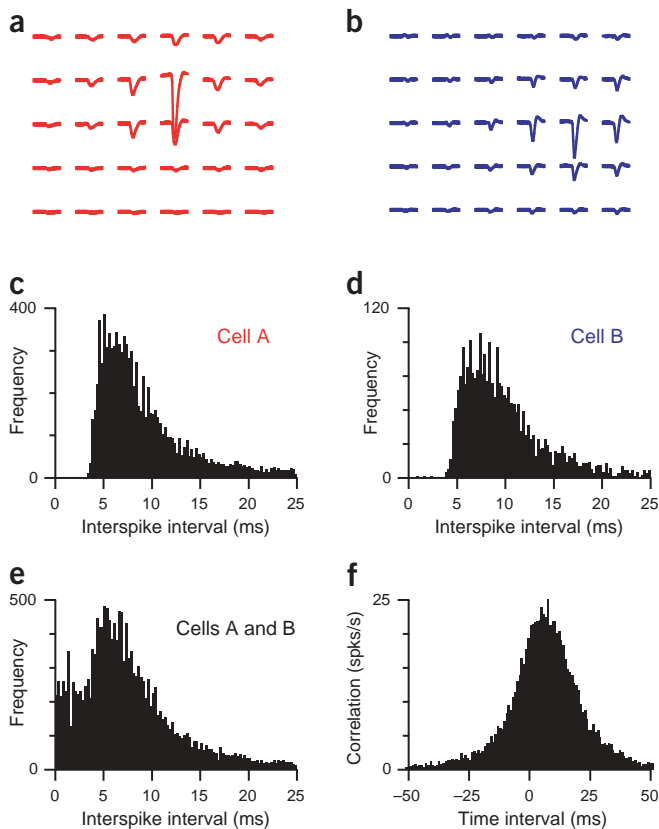


**Figure 7** Example of two nearby ganglion cells. (a,b) Average pattern of activity on the array when two different cells fire a spike. (c,d) Interspike interval distribution for the two spike trains, showing clean refractory periods. (e) Interspike interval distribution when both spike trains are combined, showing many refractory violations. (f) Cross-correlation function between the two spike trains.



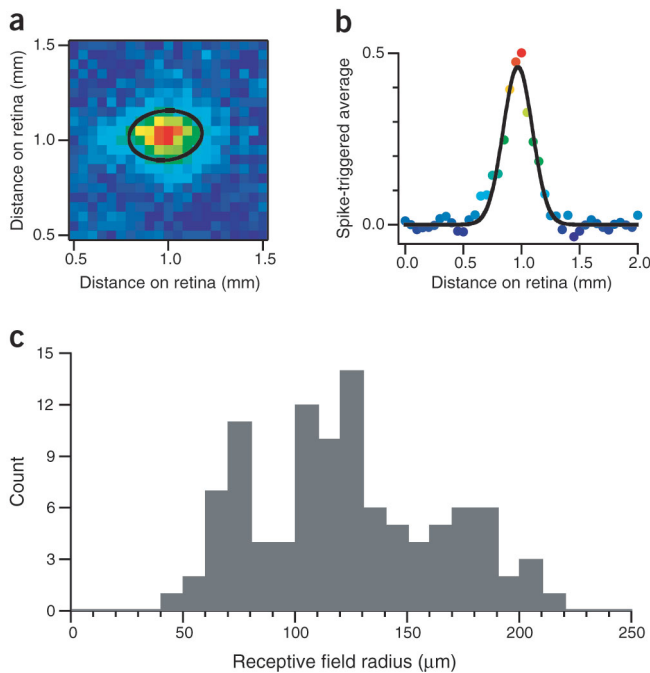


**Figure 8** Receptive field sizes of ganglion cells. (a) Spatial profile of a ganglion cell receptive field (color scale), shown with the  $1\sigma$  ellipse of a gaussian curve fit (black line). (b) One-dimensional profile of the gaussian curve fit. (c) Distribution of receptive field radii for 103 ganglion cells.

rons that are further away from the electrode and that produce a small spike or ‘spikelet’ when they fire an action potential. These spikelets introduce strong temporal correlations and highly non-gaussian statistics to the noise. Furthermore, the occurrence of spikelets can be significantly correlated with neurons that are in the vicinity of the electrode.

By using several closely spaced electrodes, ambiguous spike signals can be better discriminated. This approach was implemented first in stereotrodes (two electrodes<sup>26</sup>) and then in tetrodes (four electrodes<sup>8</sup>). So far the algorithms used for multichannel spike sorting have been a simple generalization of single-electrode methods: for example, selecting clusters from plots of peak voltage on all four electrodes<sup>8</sup>. As such, these methods do not explicitly attempt to account for overlapping spikes.

In our approach, we have combined successful elements from previous methods. We identify spike templates by using the peak voltage of a spike on many channels, as in tetrode recording<sup>8</sup>; however, we use only examples of clean spikes whose waveforms are not contaminated by overlapping spikes from other neurons. Thus, the first step of our analysis circumvents the spike overlap problem. Next, we iteratively match spike templates to putative spikes in the raw data by using a heuristic approach that is similar to the principled approach described above<sup>7</sup>. Here, we rely on the power of multichannel recording to measure a unique pattern of activity when each neuron fires a spike. Instead of making assumptions about the noise, we rely on the fact that most of the apparent noise on each electrode is explained as the occurrence of a spike measured further away. Last, by using an iterative algorithm, the computational complexity of matching each raw waveform grows linearly with the number of overlapping spikes and thus is tractable for large data sets.

**Future directions**

At present, our dense array has only 30 electrodes and a larger array would be desirable for many reasons. A multi-electrode array system with 512 channels has been built (Litke, A.M. *et al.*, *Soc. Neurosci Abstr.* 33, 429.18, 2003), showing the scalability of the array technology. For such large arrays, a significant challenge will be to automate the selection of spike templates. We have applied our methods to the favorable two-dimensional geometry of the retina; however, the basic idea of dense sampling with many electrodes can be applied to three-dimensional circuits such as the cerebral cortex. Implantable silicon ‘pin’ electrodes with many channels along their length have been developed and could be used with multichannel spike sorting algorithms to record many neurons from a local region of the cortex (ref. 27 and T.J. Blanche, P.A. Hetherington, C.J. Rennie, M.A. Spacek and N.V. Swindale, *Soc. Neurosci Abstr.* 33, 429.19, 2003). Finally, there have been many sophisticated algorithms developed for single-channel spike sorting. As our multichannel algorithm is relatively simple, it may be possible to achieve even lower rates of error by adapting some of these previous algorithms to the analysis of multichannel spike waveforms.

**METHODS**

**Electrical recording.** Experiments were done on the larval tiger salamander (*Ambystoma tigrinum*) in accordance with institutional animal care standards.

Our approach to spike sorting involves several design choices: an emphasis on recording signals from several electrodes, direct measurement of spike templates, iterative matching of templates to the raw data, and not making principled assumptions about the noise. It is important to consider these choices in the context of previous methods of spike sorting.

**Comparison to previous methods**

Many different signal processing techniques have been used to detect and to sort neural spikes on the basis of the information captured by a single electrode<sup>5,6,21–25</sup>. Most of these techniques rely on plotting two or more parameters of the spike waveform, such as its peak and width or its overlap with the first two principle components, and on choosing clusters in this low-dimensional space. Because such methods make no allowance for overlapping spikes, they are typically successful only in isolating spikes from neurons that produce large signals that are not significantly corrupted by neighboring neurons. With this approach, a hundred or more neurons have been recorded simultaneously by arrays of electrodes, but such methods capture only a small fraction of the neurons in the circuit<sup>3,4</sup>.

An algorithm for decomposing overlaps on a single electrode has been proposed<sup>7</sup>. When an overlap is detected, this algorithm compares all possible combinations of two spikes over a short range of spike occurrence times to find the combination with the highest likelihood. This approach has the drawback of being computationally expensive, particularly for three or more overlapping spikes. In addition, it requires prior knowledge of the spike rates of all of the neurons—information that is not generally available in advance. An attempt to relax the computational limitations of this procedure has been also made<sup>5,21</sup>, in which *k*-dimensional trees are used to search quickly the large space of possible combinations of spike shapes that could account for a given spike waveform.

Both of these approaches attempt to resolve the ambiguities arising from overlapping spikes in a principled way under the assumption that the noise is gaussian. It has been shown, however, that this assumption is not valid<sup>9</sup>. A chief source of noise arises from neu-



Retinas were isolated from the eye in darkness, placed with the ganglion cell layer facing a multi-electrode array (Multichannel Systems) and superfused with oxygenated (95% O<sub>2</sub>/5% CO<sub>2</sub>) Ringer's medium at room temperature (22 °C)<sup>28</sup>. Extracellularly recorded signals were digitized at 10 kSamples/s and stored for offline analysis.

**Stimulation.** Random checkerboard stimuli were displayed on a CRT monitor at a frame rate of 120 Hz and focused onto the plane of the retina using standard optics<sup>2</sup>. In this stimulus ensemble, visual space was divided into 55- $\mu$ m squares on the retina, which allowed us to fit several squares inside the receptive field center of each ganglion cell. In each square, the red, green and blue guns of the monitor were randomly and independently turned on or off every 30 ms, resulting in a light intensity and color that flickered rapidly. The mean intensity on the retina was 12 mW/m<sup>2</sup>, corresponding to photopic vision.

**Receptive field analysis.** We mapped the receptive field of each cell by calculating the average stimulus pattern preceding a spike under random checkerboard stimulation. The central region of the receptive field was identified by finding all of the squares with a time course of the same polarity as the square with the maximum response. The spike-triggered average (STA) in the central region was closely approximated as the product of three functions: the temporal dynamics  $A(t)$ , the spatial profile  $B(x,y)$  and the chromatic sensitivity  $C(I)$ <sup>3</sup>. The spatial profile  $B(x,y)$  was fitted by a two-dimensional gaussian to give the  $1\sigma$  radius,  $\sigma = (\sigma_x \sigma_y)^{1/2}$ , and area,  $A = \pi\sigma_x\sigma_y$ .

**Measuring the decay length.** Each template was normalized by its maximum amplitude, and all values at the same distance from the electrode with the maximum signal were averaged. We fitted our data with an exponential function of distance (Fig. 1c), according to ref. 8. The slope of this curve fit gave a decay length of  $28 \pm 1 \mu\text{m}$ , similar to the value found within the cortex<sup>8</sup>. The signal amplitude no longer exceeded the noise at a distance of about 80  $\mu\text{m}$ . This indicated that arrays with greater electrode spacing would not pick up signals from an individual ganglion cell on multiple electrodes, as verified with an array with an electrode spacing of 100  $\mu\text{m}$  (data not shown).

**Retrograde labeling of ganglion cells.** The eyes were removed and placed in Ringer's solution as described<sup>29</sup>, leaving an optic nerve stump of about 1 mm. A dye crystal (rhodamine dextran coupled with biotin; D-1817, molecular weight 3,000 or 10,000 Da, Molecular Probes) was placed on the optic nerve stump for at least 2 h before further processing. Biotin enhances active transport through the axon and thereby increases the loading of dye into the soma. As this dye loading was strong, we typically reduced the gain on the detector to 5% of its maximum to avoid saturation, and the fluorescence was bright enough to see clearly the dendrites of most ganglion cells (although the smaller dendrites were so densely interwoven that we could not follow these processes to their tips). Owing to their size, dye molecules did not diffuse through gap junctions to nearby ganglion and amacrine cells. As observed in other salamander species<sup>30</sup>, the ganglion cell density in the tiger salamander retina did not depend strongly on the distance from the optic disk.

**Electron microscopy of optic nerve.** We excised the optic nerves from salamanders and fixed them for 24 h at 4 °C in 3% glutaraldehyde and 6% tannic acid. Nerve tissue was post-fixed with 1% reduced osmium tetroxide in sodium cacodylate buffer with sucrose on ice for 2 h. To improve image contrast, tissues were stained *en bloc* with 1% aqueous uranyl acetate for 1 h. Finally, tissues were dehydrated by ethanol, followed by a 50/50 mixture of ethanol/propylene oxide, and infiltrated with Embed 812 resin (EM Sciences). Blocks were polymerized for 24 h and sectioned with a Diatome 35° diamond knife. Sections were placed on 1  $\times$  2 mm slot grids coated with formvar carbon. All sections were examined with a Leo 912 AB Omega energy-filtered transmission electron microscope at either 80 or 100 kV. Digital micrographs were taken with an AMT XR-60B CCD camera (Fig. 4d).

**Ganglion cell density.** Sections of the optic nerve were sampled by stepping across the whole diameter of the optic nerve and counting the number of axons in every image. This systematic sampling was required because the density of fibers was variable at the  $\times 5,000$  magnification needed to count

axons. No obvious trend was found in axon counts or axon diameters between the center and the periphery of the optic nerve. We estimated the total number of fibers in the optic nerve of the salamander to be  $42,200 \pm 3,600$  (mean  $\pm$  s.e.m.,  $n = 3$  salamanders), in close agreement with estimates made for several other species of salamanders<sup>30</sup>. The total area of the retina was  $29.7 \pm 0.63 \text{ mm}^2$  ( $n = 4$  salamanders), giving a cell density of  $1,410 \pm 180 \text{ cells/mm}^2$ . We counted labeled cells as being over the array if their somas intersected a line formed by the outer edge of the electrodes. By this definition, the rectangular array had an area of  $0.16 \times 0.13 = 0.208 \text{ mm}^2$ . Dividing the cell count by the array area gave a density of  $1,340 \pm 180 \text{ cells/mm}^2$  ( $n = 7$  experiments).

**Cross-section of the retina.** The eye was removed from the salamander, and the lens and cornea were dissected away. The tissue was fixed in 4% paraformaldehyde for 1 h and dehydrated by an overnight rinse in 30% sucrose. Cross-sections with a thickness of 10–20  $\mu\text{m}$  were cut and visualized with a Nikon phase-contrast microscope (Fig. 1c).

#### ACKNOWLEDGMENTS

We thank P. Sterling, D. Tank, A. Fairhall and S. Shoham for discussion; P. Bisher for help with confocal imaging and electron microscopy; and R. Harris and G. Lewen for assistance with data acquisition. This work was supported by a grant from the National Eye Institute (R01 EY14196) and a Pew Scholars Award to M.J.B.

#### COMPETING INTERESTS STATEMENT

The authors declare that they have no competing financial interests.

Received 16 August; accepted 2 September 2004

Published online at <http://www.nature.com/natureneuroscience/>

- Rodieck, R.W. *The First Steps in Seeing* (Sinauer Associates, Sunderland, Massachusetts, USA, 1998).
- Meister, M., Pine, J. & Baylor, D.A. Multi-neuronal signals from the retina: acquisition and analysis. *J. Neurosci. Methods* **51**, 95–106 (1994).
- Schnitzer, M.J. & Meister, M. Multineuronal firing patterns in the signal from eye to brain. *Neuron* **37**, 499–511 (2003).
- DeVries, S.H. & Baylor, D.A. Mosaic arrangement of ganglion cell receptive fields in rabbit retina. *J. Neurophysiol.* **78**, 2048–2060 (1997).
- Lewicki, M.S. A review of methods for spike sorting: the detection and classification of neural action potentials. *Network* **9**, R53–R78 (1998).
- Hulata, E., Segev, R. & Ben-Jacob, E. A method for spike sorting and detection based on wavelet packets and Shannon's mutual information. *J. Neurosci. Methods* **117**, 1–12 (2002).
- Atiya, A.F. Recognition of multiunit neural signals. *IEEE Trans. Biomed. Eng.* **39**, 723–729 (1992).
- Gray, C.M., Maldonado, P.E., Wilson, M. & McNaughton, B. Tetrodes markedly improve the reliability and yield of multiple single-unit isolation from multi-unit recordings in cat striate cortex. *J. Neurosci. Methods* **63**, 43–54 (1995).
- Fee, M.S., Mitra, P.P. & Kleinfeld, D. Automatic sorting of multiple unit neuronal signals in the presence of anisotropic and non-gaussian variability. *J. Neurosci. Methods* **69**, 175–188 (1996).
- Henze, D.A. *et al.* Intracellular features predicted by extracellular recordings in the hippocampus *in vivo*. *J. Neurophysiol.* **84**, 390–400 (2000).
- Watt, C.B., Yang, S.Z., Lam, D.M. & Wu, S.M. Localization of tyrosine-hydroxylase-like-immunoreactive amacrine cells in the larval tiger salamander retina. *J. Comp. Neurol.* **272**, 114–126 (1988).
- Zhang, J. & Wu, S.M. Immunocytochemical analysis of cholinergic amacrine cells in the tiger salamander retina. *NeuroReport* **12**, 1371–1375 (2001).
- Zhang, J., Yang, Z. & Wu, S.M. Immunocytochemical analysis of spatial organization of photoreceptors and amacrine and ganglion cells in the tiger salamander retina. *Vis. Neurosci.* **21**, 157–166 (2004).
- Sakai, H.M., Machuca, H. & Naka, K.I. Processing of color- and noncolor-coded signals in the gourami retina. II. Amacrine cells. *J. Neurophysiol.* **78**, 2018–2033 (1997).
- Cleland, B.G. & Levick, W.R. Brisk and sluggish concentrically organized ganglion cells in the cat's retina. *J. Physiol. (Lond.)* **240**, 421–456 (1974).
- Cleland, B.G. & Levick, W.R. Properties of rarely encountered types of ganglion cells in the cat's retina and an overall classification. *J. Physiol. (Lond.)* **240**, 457–492 (1974).
- Toris, C.B., Eiesland, J.L. & Miller, R.F. Morphology of ganglion cells in the neotenuous tiger salamander retina. *J. Comp. Neurol.* **352**, 535–559 (1995).
- Sun, W., Li, N. & He, S. Large-scale morphological survey of mouse retinal ganglion cells. *J. Comp. Neurol.* **451**, 115–126 (2002).
- Rockhill, R.L., Daly, F.J., MacNeil, M.A., Brown, S.P. & Masland, R.H. The diversity of ganglion cells in a mammalian retina. *J. Neurosci.* **22**, 3831–3843 (2002).
- Wässle, H. & Boycott, B.B. Functional architecture of the mammalian retina. *Physiol. Rev.* **71**, 447–480 (1991).

21. Lewicki, M.S. Bayesian modeling and classification of neural signals. *Neural Comput.* **6**, 1005–1030 (1994).
22. Hulata, E., Segev, R., Shapira, Y., Benveniste, M. & Ben-Jacob, E. Detection and sorting of neural spikes using wavelet packets. *Phys. Rev. Lett.* **85**, 4637–4640 (2000).
23. Wheeler, B.C. & Smith, S.R. High-resolution alignment of action potential waveforms using cubic spline interpolation. *J. Biomed. Eng.* **10**, 47–53 (1988).
24. Yang, X.W. & Shamma, S.A. A totally automated system for the detection and classification of neural spikes. *IEEE Trans. Biomed. Eng.* **35**, 806–816 (1988).
25. Wheeler, B.C. & Brewer, G.J. Multineuron patterning and recording. *Enabling Technologies for Culturing Neural Networks* (eds. Stenger, D.A. & McKenna, T.M.) 167–185 (Academic, San Diego, California, USA, 1994).
26. McNaughton, B.L., O'Keefe, J. & Barnes, C.A. The stereotrode: a new technique for simultaneous isolation of several single units in the central nervous system from multiple unit records. *J. Neurosci. Methods* **8**, 391–397 (1983).
27. Vetter, R.J., Williams, J.C., Hetke, J.F., Nunamaker, E.A. & Kipke, D.R. Chronic neural recording using silicon-substrate microelectrode arrays implanted in cerebral cortex. *IEEE Trans. Biomed. Eng.* **51**, 896–904 (2004).
28. Balasubramanian, V. & Berry, M.J. A test of metabolically efficient coding in the retina. *Network* **13**, 531–552 (2002).
29. Dacey, D.M., Peterson, B.B., Robinson, F.R. & Gamlin, P.D. Fireworks in the primate retina: *in vitro* photodynamics reveals diverse LGN-projecting ganglion cell types. *Neuron* **37**, 15–27 (2003).
30. Roth, G. *Visual Behavior in Salamanders* (Springer, Berlin, 1987).